



Linear-dendritic drug conjugates forming long-circulating nanorods for cancer-drug delivery



Zhuxian Zhou^b, Xinpeng Ma^b, Erlei Jin^b, Jianbin Tang^a, Meihua Sui^a, Youqing Shen^{a,b,*}, Edward A. Van Kirk^c, William J. Murdoch^c, Maciej Radosz^b

^aCenter for Bionanoengineering and State Key Laboratory for Chemical Engineering, Department of Chemical and Biological Engineering, Zhejiang University, Hangzhou 310027, China

^bDepartment of Chemical and Petroleum Engineering, University of Wyoming, Laramie, WY 82071, United States

^cDepartment of Animal Science, University of Wyoming, Laramie, WY 82071, United States

ARTICLE INFO

Article history:

Received 25 February 2013

Accepted 4 April 2013

Available online 29 April 2013

Keywords:

Cancer-drug delivery
Linear-dendritic polymer
Drug conjugate
Self-assembly
Nanorods
Camptothecin

ABSTRACT

Elongated micelles have many desirable characteristics for cancer-drug delivery, but they are difficult to obtain since amphiphilic polymers form such nanostructures only within narrow composition ranges depending on their own structures. Herein, we demonstrated a facile fabrication of different nanostructures via drug content-controlled self-assembly of amphiphilic linear-dendritic drug conjugates – using the number of the conjugated hydrophobic drug molecule camptothecin (CPT) to tailor the hydrophobicity of amphiphilic PEG-*block*-dendritic polylysine–CPT (PEG-*x*CPT) conjugates and thereby control their self-assembled nanostructures – nanospheres or nanorods of different diameters and lengths. The shape and size of the nanostructures were found to strongly affect their *in vitro* and *in vivo* properties, particularly the blood clearance kinetics, biodistribution and tumor targeting. The nanorods with medium lengths (<500 nm) had a much longer blood circulation and faster cellular uptake than the nanospheres or long nanorods. Thus, polymeric nanorods with proper lengths may be ideal nanocarriers capable of uniting the opposite requirements in cancer-drug delivery.

© 2013 Elsevier Ltd. All rights reserved.

1. Introduction

Spherical [1–4] or wormlike micelles [5–7] and vesicles [8–10] from self-assembly of amphiphilic polymers have been extensively explored as nanocarriers for cancer-drug and gene delivery. These polymeric nanocarriers significantly improve drugs' solubility and promote their accumulation in tumor tissues via the enhanced permeability and retention (EPR) effect [11], in which the nanocarriers extravasate through the tumor's highly permeable blood vessels into tumor tissue and are trapped there due to its lack of lymphatic drainage [12,13]. Prolonging the nanocarriers' blood circulation increases their opportunity to pass through the leaky vasculature, and thereby their extravagation into tumor tissue [14]. Surface properties and nanocarrier size are the two important

factors affecting their blood circulation times [15–19]. Recently, the nanocarrier shape has been recognized as another important parameter [5–7,20–22]. For instance, Discher et al. found that flexible worm-like micelles could circulate in the blood for a week [5–7], much longer than their spherical counterparts. Dai et al. found that carbon nanotubes pegylated with long PEG chains had a long circulation ($t_{1/2} = 22.1$ h) in mice [21].

The drug retention, cellular uptake ability, and intracellular release profile of the nanocarrier, however, are equally important for effective tumor drug accumulation [23]. Most micellar or particulate nanocarriers, which are loaded with drugs by hydrophobic interaction-based physical trapping, suffer a premature-burst release problem: A large fraction of the carried drugs (up to 40–60%) is quickly released once in the medium. For instance, PCL worm micelles released ~40% of their drug in the first few hours [24]. Thus, after the initial burst drug release such nanocarriers carry little drugs to the tumor even if they circulate very long in the bloodstream and finally accumulate in the tumor. On the other hand, once in the tumor, the nanocarriers must be quickly taken up by tumor cells and quickly release their drugs intracellularly to exert pharmaceutical actions [25]. The properties endowing the

* Corresponding author. Center for Bionanoengineering and State Key Laboratory for Chemical Engineering, Department of Chemical and Biological Engineering, Zhejiang University, Hangzhou 310027, China. Fax: +86 571 87953993.
E-mail address: shenyq@zju.edu.cn (Y. Shen).

nanocarriers with stealth and long circulation now slow their cellular uptake by tumor cells. For instance, the cellular uptake of wormlike particles was found to be much slower than that of spherical nanoparticles due to their shape-induced inhibition of phagocytosis [26–28]. Thus, a nanocarrier must *simultaneously* meet disparate requirements to achieve high therapeutic efficacy: good stealth property and strong drug retention while in the blood circulation, but fast cellular uptake and intracellular release once in tumor tissue [23,29].

PEGylated metallic and inorganic nanorods [30,31] as models were demonstrated to have long circulation times like wormlike micelles [5–7] and the ability to penetrate tumor efficiently via the enhanced pore transportation [32] and fast cellular uptake [33–35] compared to nanospheres. However, they cannot be used clinically for intravenous drug delivery. Biodegradable polymeric nanorods may also possess these essential characteristics and would be suitable for *in vivo* drug delivery. Unfortunately, like wormlike micelles, amphiphilic copolymers form rod-like morphology only within very narrow composition ranges (i.e., hydrophilic/hydrophobic ratios), and also depend on the nature of the polymers [36,37]. For instance, flexible linear PEG-block copolymers such as PEG–PCL and PEG–PLA formed flexible worm-like micelles at certain hydrophilic/hydrophobic ratios [36,38–40] due to their fluid cores [41,42]. Furthermore, even if an amphiphilic polymer itself can form such a rod nanostructure, drug loading or

conjugation may disrupt the nanostructure formation because it changes the polymer composition or amphiphilicity. Thus, an extensive fine-tuning of those parameters, including the polymer structure, composition and the drug content, would be required to obtain a polymer to form drug-loaded nanorods. To date, there are no reports on the fabrication of polymeric nanorods for drug delivery.

Now that many anticancer drugs are hydrophobic, we proposed to directly use the hydrophobic drugs as the hydrophobic moiety of amphiphilic polymers, and thus we could simply tune their drug contents to control the self-assembled nanostructures of the resulting amphiphilic polymers. Another advantage of this approach is that the resulting nanocarriers would have high drug loading contents and be free of premature drug release. The disulfide linker used for drug conjugation would enable the nanorods to retain the drug tightly in the circulation but quickly release the drug once in cancer cells by responding to the intracellular glutathione [43]. Herein, we demonstrate such a hydrophobic drug content-controlled self-assembly of linear-dendritic drug conjugates to fabricate polymeric nanostructures. By directly using the conjugated hydrophobic drug molecule (camptothecin, CPT) to tailor the amphiphilicity of PEG-*block*-dendritic polylysine–CPT (PEG–x CPT) conjugates and thereby control their self-assembly, nanostructures—nanospheres or nanorods of different diameters and lengths were obtained (Fig. 1).

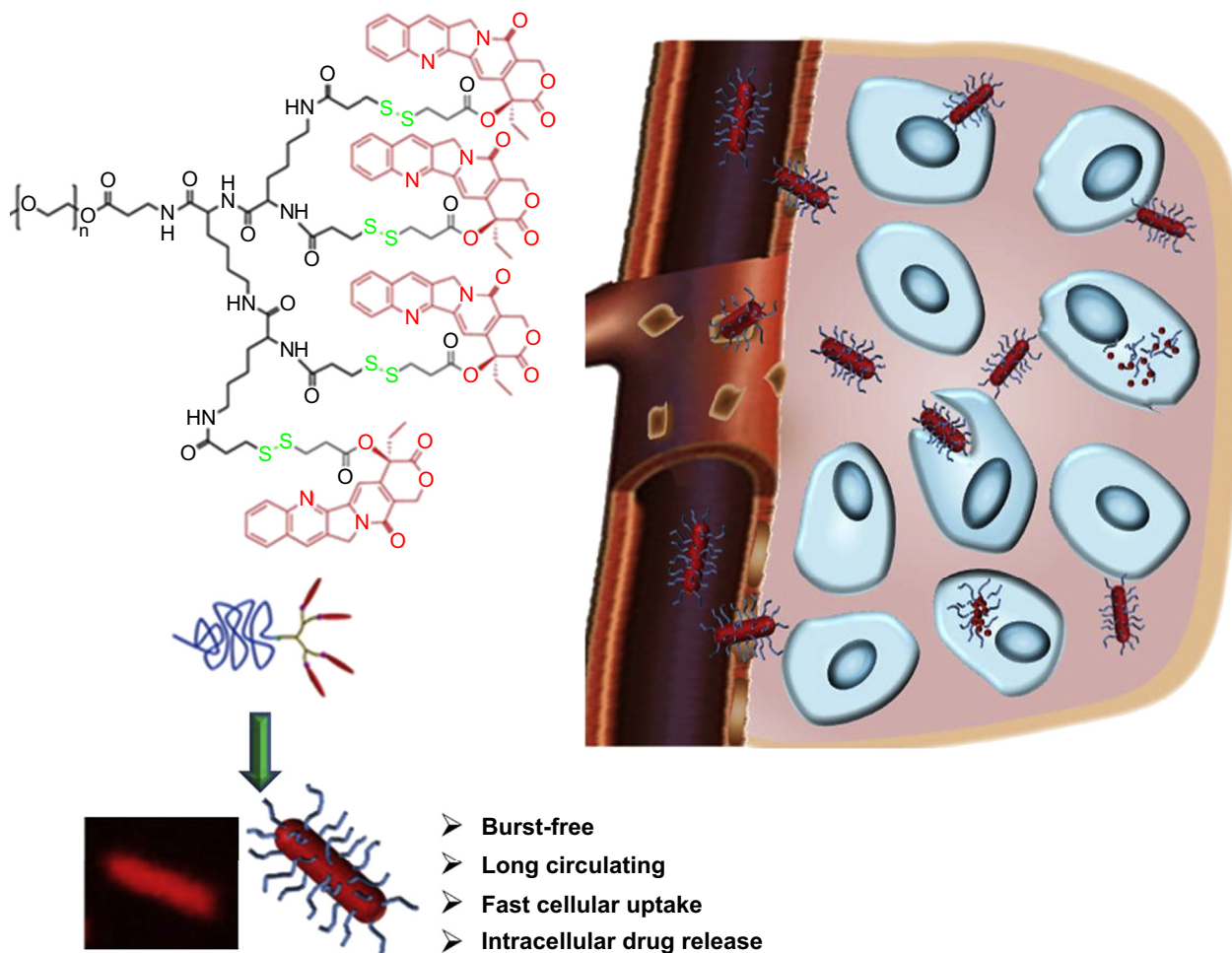


Fig. 1. Self-assembly of PEG-dendritic polylysine–camptothecin (PEG–x CPT) conjugates into biodegradable nanospheres or nanorods with high drug loading: The formation of the morphologies was determined by the generation of the dendritic polylysine and the number of the conjugated CPT. Nanorods with short length (<500 nm) have characteristics of long blood circulating, fast cellular internalization, and intracellular drug release.

2. Materials and methods

2.1. Materials

Poly(ethylene glycol) methyl ether ($M_n = 2000$), *N*-(*tert*-butoxycarbonyl)glycine (Boc-Gly-OH), *N,N*-dicyclohexylcarbodiimide (DCC), 4-(dimethylamino)pyridine (DMAP), *N,N*-diisopropylethylamine (DIEA), (S)-(+)-camptothecin (CPT) were purchased from Sigma–Aldrich, USA. Boc-Lys(Boc)-OH was purchased from Fisher Scientific Inc. 2,3,4,5,6-Pentafluorophenol (PFP), *N*-(3-dimethylaminopropyl)-*N*-ethylcarbodiimide hydrochloride (EDC) and trifluoroacetic acid (TFA) were purchased from Oakwood Products Inc., USA. All the chemicals were used as received. *N*-Succinimidyl 3-(2-pyridyldithio) propionate (SPDP) was synthesized according to the literature [44].

2.2. Synthesis of linear-dendritic PEG–DPLL–camptothecin conjugates (PEG–xCPT)

2.2.1. Synthesis of PEG₄₅–dendritic polylysines (PEG–DPLL)

PEG₄₅–dendritic polylysines of different generations were synthesized using a reported method [45]. Briefly, H₃CO–PEG–OH ($M_n = 2000$) was coupling with Boc-Gly-OH by DCC in dichloromethane. The protecting group was removed with CH₂Cl₂ and TFA (1:1) to obtain PEG₄₅–NH₂. TFA (PEG₄₅–DPLL G₀). The active ester Boc-Lys(Boc)-OPFP was prepared via the reaction of Boc-Lys(Boc)-OH and PFP with DCC in dioxane. PEG₄₅–DPLL G₁ was generated by PEG₄₅–NH₂–TFA coupling with Boc-Lys(Boc)-OPFP followed by deprotection with CH₂Cl₂/TFA (1:1). PEG₄₅–DPLL G₂ and PEG₄₅–DPLL G₃ were obtained by repeated coupling with Boc-Lys(Boc)-OPFP and deprotection.

2.2.2. Preparation of CPT–PDP

CPT-SH was synthesized as we reported previously [43]. CPT-SH (1 g, 2.3 mmol) was dissolved in dichloromethane (30 mL) followed by the addition of SPDP (1.04 g, 3.4 mmol). The mixture was stirred at room temperature for 3 h, and some CPT–PDP precipitated out from the solution. Thin-layer chromatography (CHCl₃:MeOH = 1:0.05) was used to confirm all CPT-SH was reacted. The mixture was then concentrated and poured into ethyl ether. The precipitate was isolated and dried in vacuum to obtain a light yellow solid, yielding 93%. ¹H NMR (400 MHz, CDCl₃, δ) of CPT–PDP: 8.42 (s, 1H), 8.26 (d, 1H), 7.97 (d, 1H), 7.88 (m, 1H), 7.69 (m, 1H), 5.73 and 5.45 (m, 2H), 5.32 (s, 2H), 3.02 (m, 4H), 2.89 (m, 4H), 2.33 and 2.22 (m, 2H), 1.01 (t, 3H).

2.2.3. Preparation of PEG₄₅–OctaCPT (Fig. 2)

PEG₄₅–G₃ (100 mg, 0.2 mmol NH₂) and DIEA (52 μL, 0.3 mmol) were dissolved in DMSO (4 mL) under N₂. CPT–PDP (133 mg, 0.21 mmol) dissolved in DMSO (4 mL) was then added to the solution under N₂. The mixture was stirred for 4 h and then dialyzed (Spectra/Pro MWCO = 1000) against acetonitrile (100 mL). The precipitate was collected and washed with acetonitrile (10 mL × 3) until no free CPT was found in thin-layer chromatography (TLC) (CHCl₃:MeOH = 1:0.1). The solid was dried in vacuum to give PEG₄₅–OctaCPT, yielding 85%. PEG₄₅–CPT, PEG₄₅–DiCPT, and PEG₄₅–TetraCPT were synthesized similarly. For PEG₄₅–CPT and PEG₄₅–DiCPT, there was no precipitation during the dialysis step. The yield of PEG₄₅–CPT, PEG₄₅–DiCPT, and PEG₄₅–TetraCPT was 90%, 88%, and 78%, respectively.

2.3. Reverse-phase HPLC

Ion-pairing reverse-phase HPLC (RP-HPLC) was performed on an RP-C18 HPLC column (250 × 4.6 mm², 5 μm). Isocratic elution characterized the products and the drug biodistribution *in vivo*. Eluant A was water containing 0.05% TFA and B was acetonitrile containing 0.05% TFA. The mobile phase for isocratic elution was run with 50% A and 50% B at a flow rate of 1.3 mL/min for 20 min. The volume of each injection was 100 μL, and the detection of eluted samples was performed at 360 nm. A CPT standard curve was generated using CPT solutions ranging from 6.25 to 50 μg/mL with good linearity and a correlation coefficient of 0.9999.

2.4. Preparation of the spherical- and rod-like nanoparticles

PEG–xCPT conjugates were dissolved in DMF (0.5 mL) at a designed concentration. The solution was filtered through a PTFE filter (pore size 0.45 μm). Milli-Q deionized water (1 mL) was slowly added dropwise to the solution with stirring. The solution was then dialyzed against water or PBS (Spectra/Por, MWCO = 3500, 24 h, 1 L × 4) to remove DMF. The DOX-loaded spherical- and rod-like nanoparticles were fabricated using the same procedure except for adding DOX·HCl (0.5 mg) and DIEA (2 μL) to the solution. The DOX-loading content was determined by measuring its UV absorbance at 486 nm in DMSO/methanol.

2.5. Matrix-assisted laser desorption/ionization time-of-flight mass spectrometry (MALDI-TOF MS)

α-Cyano-4-hydroxycinnamic acid was used as the matrix for MALDI-TOF MS measurements. The matrix was prepared at a concentration of 10 mg/mL in THF. The sample solution (1 μL) was applied to the MALDI sample plate and dried. The matrix solution (1 μL) was then added to the plate and dried. The instrument was operated

in a linear mode. A N₂ laser operating at 337 nm with 3 ns pulses was used. The ions generated by the laser pulses were accelerated to 20 kV.

2.6. Dynamic laser light scattering (DLS)

The sizes (diameters) of the CPT-conjugated nanoparticles were determined using a Nano-ZS Zetasizer (Malvern Instrument Ltd., UK) with a laser light wavelength of 632.8 nm and a scattering angle at 173°. The nanoparticles were prepared as described above. The zetasizer was routinely calibrated with a 60 nm nanosphere™ standard (Duke Scientific Corp., CA). Each measurement was performed in triplicate, and the results were processed with DTS software version 3.32.

2.7. Transmission electron microscopy (TEM) of the nanoparticles

The nanoparticle solution (1 mg/mL, 10 μL) was applied onto a 150-mesh carbon-coated copper grid. The excess solution was wicked off with filter paper. A droplet of 1% (w/v) aqueous uranyl acetate solution was then deposited onto the dried samples. The excess solution of the staining agent was sucked away using filter paper from the edge of the TEM grids. Images were recorded using a transmission electron microscope (HITACHI H-7000 TEM) operated at a voltage of 75 kV.

2.8. Observing the nanoparticles by confocal laser scanning fluorescence microscopy

The nanoparticles were visualized with confocal microscopy using Nile red as the fluorescent dye. PEG–xCPT (2 mg/mL) containing Nile red (20 μg/mL) in DMF was dialyzed against (Spectra/Por, MWCO = 3500) water (24 h, 1 L × 4), producing nanoparticles loaded with Nile red. The images were taken using a Zeiss 710 confocal microscope. Nile red was excited using a 561-nm laser, and the emission wavelength was read from 590 to 610 nm and expressed as red.

2.9. Critical micelle concentration (CMC) determination

The CMC of PEG–xCPT was determined using a method reported before [46]: A stock solution of the PEG–xCPT (2 mg/mL) was prepared in 10 mM pH 7.4 phosphate buffer. Nile red in CH₂Cl₂ (10 μL, 0.5 mg/mL) was added to a series of vials and the CH₂Cl₂ was evaporated. The polymer solution and 10 mM pH 7.4 phosphate buffer were added to vials to obtain the polymer concentrations ranging from 0.00195 to 2 mg/mL. The vials were then stirred at room temperature for 6 h for equilibration. The fluorescence emission of each solution was measured. The CMC was determined as the intersection of the tangents to the two linear portions of the plot of the emission intensity as a function of the polymer concentration.

2.10. Cell culture

MCF-7 and MCF-7/ADR breast cancer cells were purchased from American Type Culture Collection (ATCC, Manassas, VA). Cells were cultured in RPMI-1640 medium containing 10% fetal bovine serum (FBS), 10 μg/mL insulin, and 1% antibiotic/antimycotic solution (Sigma A9909) at 37 °C in 5% CO₂ environment.

2.11. Cellular uptake of the nanoparticle

Cellular uptake of the DOX-loaded nanoparticles was observed using confocal fluorescence microscopy. Cells were incubated with the free DOX or DOX-loaded nanoparticles (DOX concentration: 4 μg/mL) at 37 °C and 5% CO₂ for 1, 4 or 8 h. The cells were then thoroughly washed with PBS at 4 °C three times. Images were obtained using a Leica TCS SP2 microscope. DOX was observed using an Ar/ArKr 458/488 nm laser and the emission wavelength was read from 560 to 610 nm and expressed as red. Images were produced using the lasers sequentially with a 40× objective lens. Cells were kept at 37 °C and 5% CO₂ except when being observed on the microscope. Images were processed with NIH ImageJ.

2.12. Flow cytometry

Cells were seeded onto twelve-well plates (2.0 mL of cell suspension per well) at 2×10^5 cells mL⁻¹ and allowed to grow for 24 h. DOX and DOX-loaded nanoparticles were added to each well and incubated with cells for 1, 4, or 8 h. The cells were then washed with cold PBS twice, harvested by 0.005% trypsin–EDTA, pelleted in eppendorfs and centrifuged at 1000 g for 4 min at 4 °C, and then resuspended in PBS with 2% FBS and filtered through cell strainers. Each sample was quickly analyzed on a BD LSRII flow cytometer (BD Biosciences, San Jose, CA) using the 488 laser for excitation and the emitted 525/50 fluorescence for detection. Files were collected of 10,000 gated events and analyzed with FlowJo 7.6.5 software.

2.13. *In vitro* cytotoxicity assay

The cytotoxicity assay was carried out using the MTT cell proliferation assay kit (ATCC, Manassas, VA) according to the modified manufacturer's protocol. MCF-7 or MCF-7/ADR cells were seeded onto 96-well plates and incubated for 24 h. The original medium (200 μL) was removed and replaced with the PEG–xCPT or free CPT

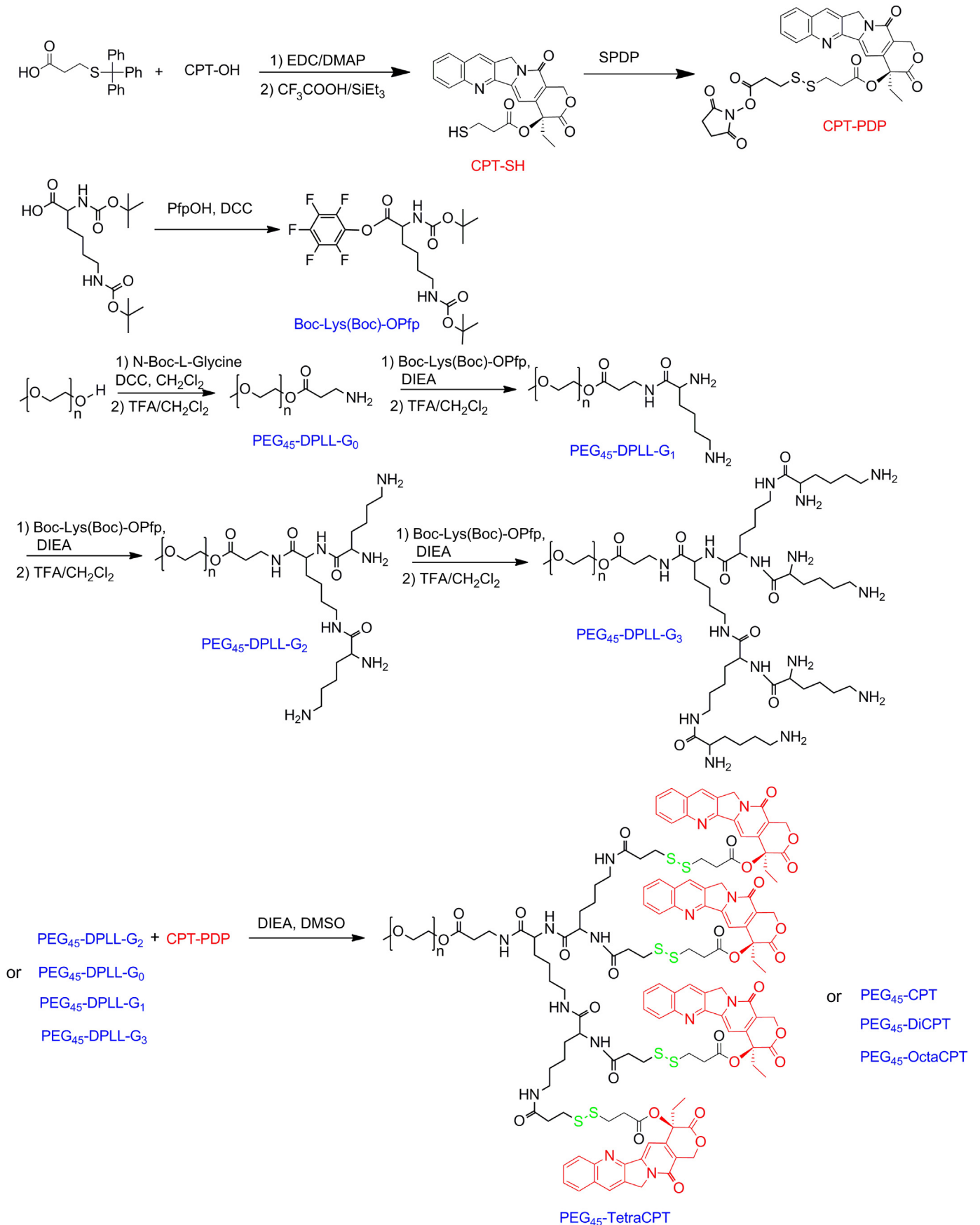


Fig. 2. Synthesis of linear-dendritic PEG-DPLL-camptothecin conjugates (PEG-xCPT) via a disulfide linker.

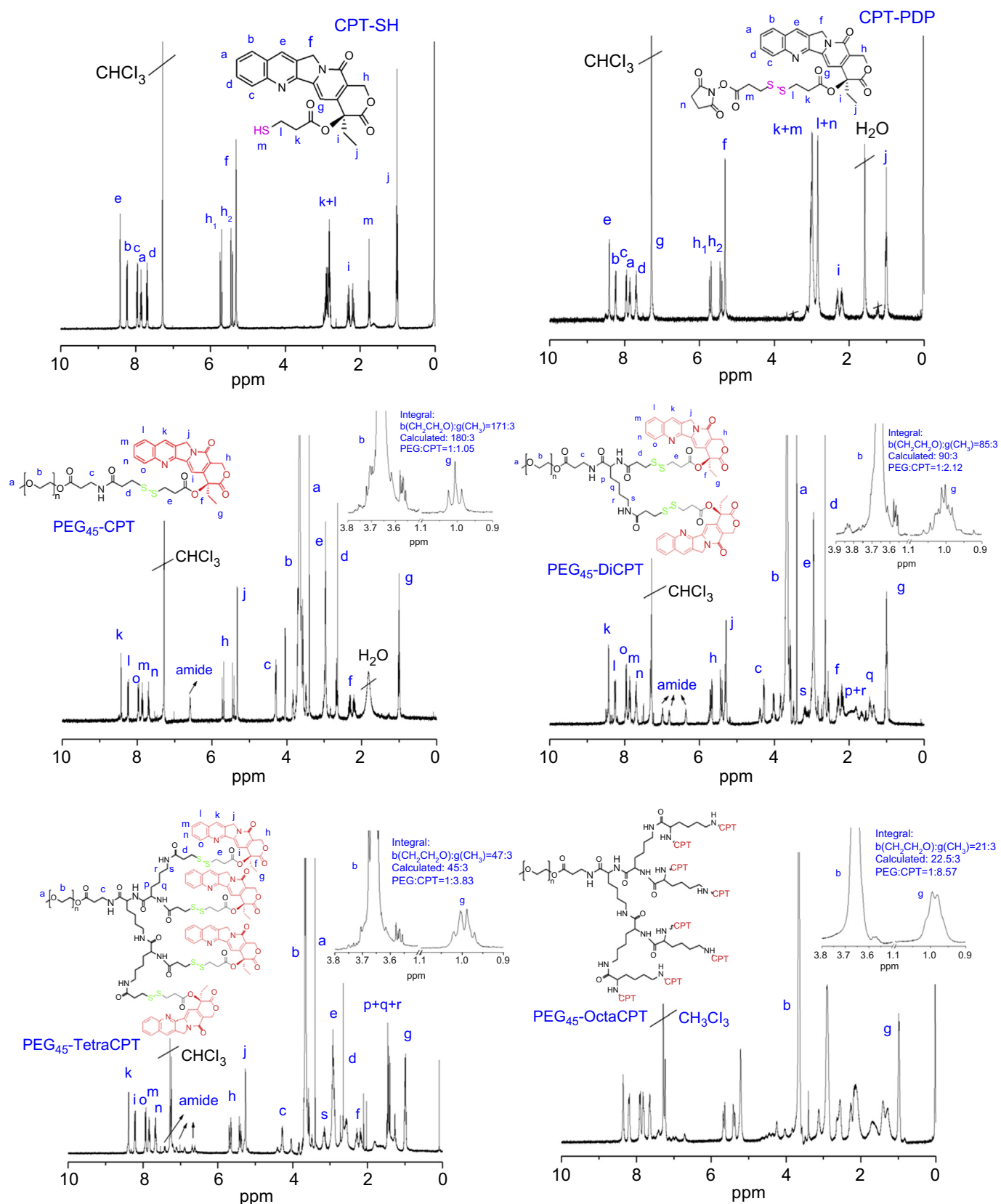


Fig. 3. The ¹H NMR spectra of CPT-SH, CPT-PDP, and PEG₄₅-xCPT in CDCl₃.

solutions at different concentrations and incubated for 72 h. The medium in each well was then replaced with 100 μL fresh cell culture medium. MTT reagent (10 μL) was then added to each well and incubated for 6 h until purple precipitates were visible. Finally, the detergent reagent (100 μL) was added to each well, and the plates were incubated at 37 $^{\circ}\text{C}$ for 18 h or until all the crystals were dissolved. The absorbance intensity at 570 nm was recorded and the cytotoxicity was expressed as a percentage of the control.

2.14. Animals

BALB/c mice (Charles River Laboratories, Wilmington, MA, USA) were maintained in compliance with the policy on animal care expressed in the National Research Council guidelines and all experiments were approved and supervised by the Institutional Animal Care and Use Committee (IACUC) at the University of Wyoming (WY, USA). Mice were maintained in a pathogen-free environment under controlled temperature (24 $^{\circ}\text{C}$) and lighting (12 L:12 D) conditions. Autoclaved rodent chow and sterilized water were supplied *ad libitum*.

2.15. Blood circulation and biodistribution studies in Balb/C mice

Mice were injected intravenously via the tail vein (four mice per group) with PEG-xCPT (PEG₄₅-DiCPT, PEG₄₅-TetraCPT or PEG₄₅-OctaCPT, 10 mg CPT-eq./kg) in 100 μL PBS solution. 100 μL of blood was collected (5 min, 1 h, 4 h, and 8 h) and the blood was mixed with heparin in eppendorfs. After 4 or 24 h, the mice were sacrificed and the blood (collected via the orbital sinus), liver, kidney, muscle, gut,

spleen, heart, lung, and brain tissues were collected for analyses. Tissues were weighed (100–200 mg) and homogenized in 0.5 mL PBS. DTT (10 mM) was then added to the collected blood or homogenized tissues and then incubated at 4 $^{\circ}\text{C}$ overnight. All samples were stored at -80°C until measurements could be made. At measurement time, the samples were thawed, and 400 μL acetonitrile was added to the blood or homogenized tissue solutions (100 μL) in PBS. The mixtures were vortexed and kept at RT for 1 h followed by centrifuging for 5 min at 14,000 rpm. Finally, 200 μL of the supernatant was then analyzed by HPLC. The CPT content was calculated according to the standard curve.

2.16. In vivo fluorescence imaging

The mice were implanted in the mammary pad with 5×10^5 4T1-Luc cells in 50 μL PBS. To monitor the growth of the 4T1-Luc breast tumors, the mice were intraperitoneally injected with D-luciferin (200 μL in PBS, 15 mg/mL). Ten minutes following the injection, mice were anesthetized with 2% isoflurane and imaged on a Xenogen IVIS Lumina system (Caliper Life Sciences, Hopkinton, MA). The study was performed when the tumor size reached 0.5–1.0 cm in diameter in about two weeks. DOX-loaded nanoparticles in PBS were injected via the tail vein at a dose of 5 mg DOX-eq./kg. The mice were sacrificed at 8 h post-injection. Tumors and major organs, including liver, heart, spleen, kidney, and lung were dissected, washed with PBS and imaged on the Maestro FLEX *In Vivo* imaging system (blue: excitation, 500–720 nm; exposure time 600 ms). The DOX signal was spectrally extracted from the multi-spectral fluorescence images with Maestro software (Cambridge Research & Instrumentation, Inc., Woburn, MA) after subtracting the background auto-fluorescence.

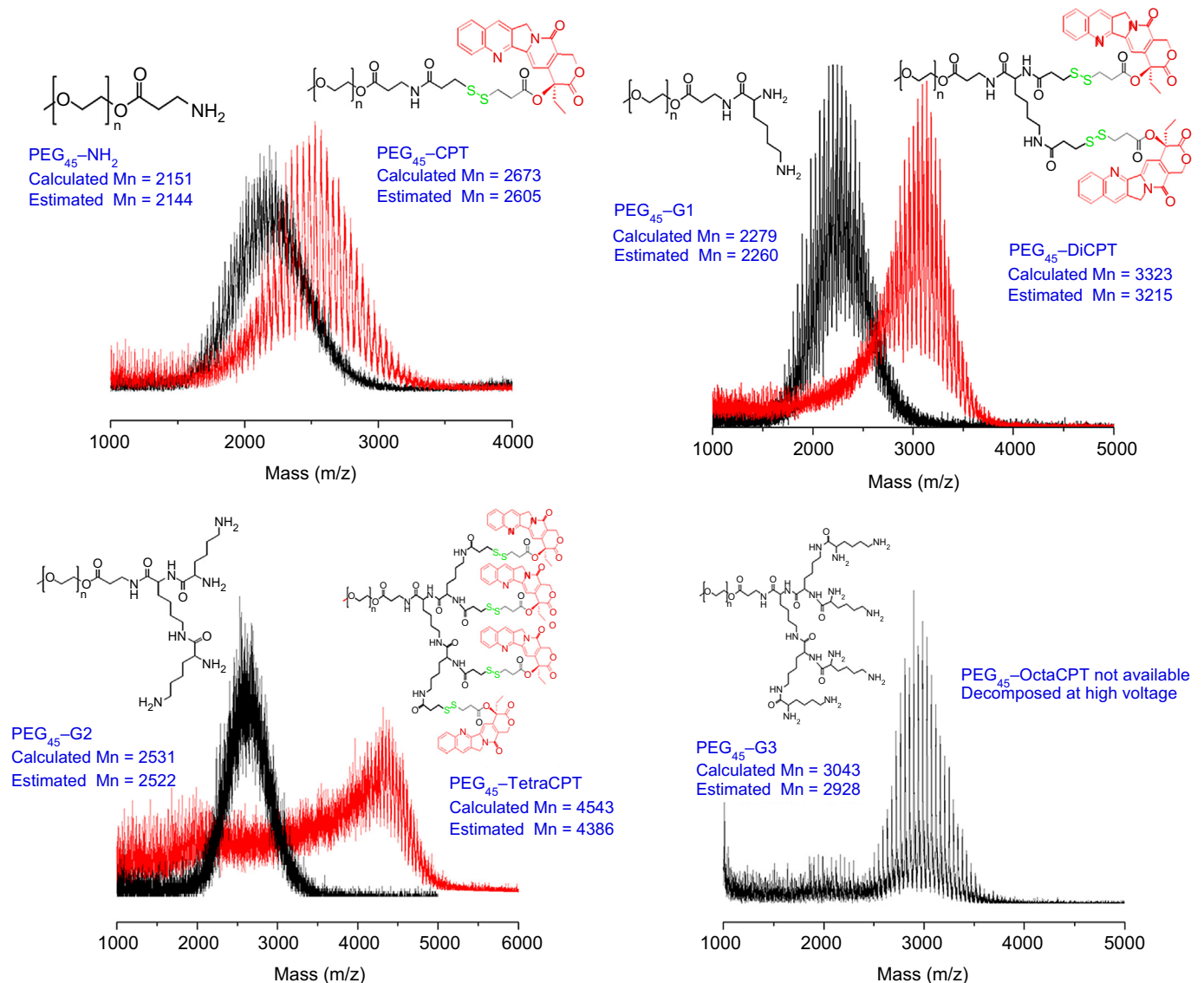


Fig. 4. The MALDI-TOF MS spectra of the linear-dendritic PEG-DPLL copolymers and the corresponding conjugates PEG₄₅-x-CPT. PEG₄₅-OctaCPT decomposed during the measurement and only PEG₄₅-DPLL (G₃) is shown.

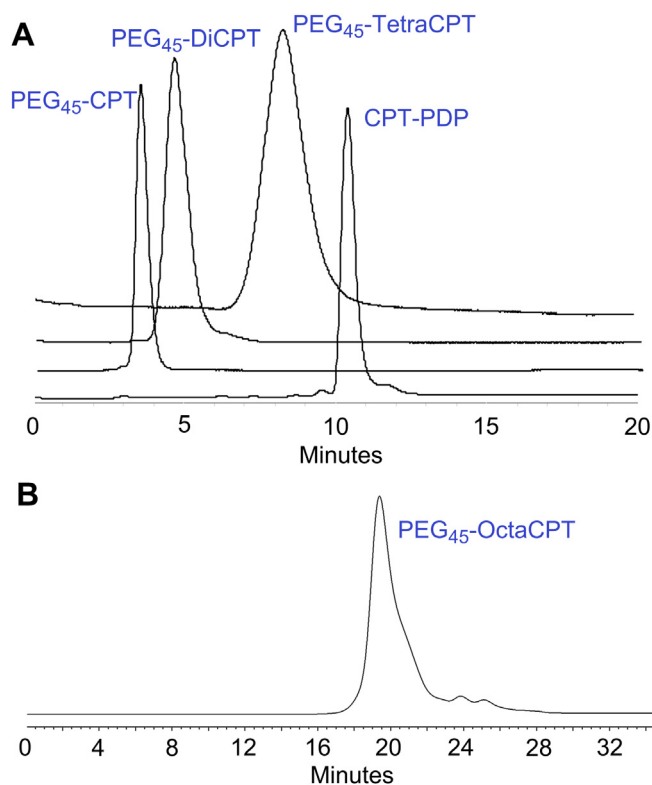


Fig. 5. (A) The HPLC traces of CPT–PDP, PEG₄₅–CPT, PEG₄₅–DiCPT and PEG₄₅–TetraCPT. Conditions: Eluant A was water containing 0.05% TFA and B was acetonitrile containing 0.05% TFA. The mobile phase for isocratic elution was run with 50% A and 50% B at a flow rate of 1.3 mL/min for 20 min. (B) The GPC trace of PEG₄₅–OctaCPT. GPC conditions: DMF as a solvent; column temperature 50 °C.

3. Results

3.1. Synthesis and characterization of PEG–x CPT conjugates

The synthesis of PEG–x CPT conjugates is shown in Fig. 2. CPT–PDP containing a disulfide bond and an NHS active ester group was first synthesized. PEG–block–dendritic PLL (DPLL) of different generations was prepared and then reacted with a corresponding amount of CPT–PDP to obtain PEG–DPLL conjugated with 1, 2, 4, or 8 CPT molecules. The structures of the conjugates were characterized by ¹H NMR spectra (Fig. 3), MALDI–TOF MS spectra (Fig. 4), HPLC (Fig. 5A) and GPC (Fig. 5B). The molecular weights measured by MALDI–TOF MS spectra were 2605, 3215, and 4386 Da for PEG₄₅–CPT, PEG₄₅–DiCPT, and PEG₄₅–TetraCPT, respectively, agreeable with their theoretical values. The MALDI–TOF MS spectrum of PEG₄₅–OctaCPT was not obtained due to its decomposition at high voltages. Its molecular weight measured by GPC was 6853 (theoretical value: 7143). The number of CPT molecules in each conjugate, calculated from its ¹H NMR spectrum from the integration ratio of the peaks at 3.58 ppm (–CH₂CH₂O–, PEG) and 1.01 ppm (–CH₃, CPT), was 1.05 for

Table 1
Summary of the characterizations and properties of PEG–x CPT conjugates.

PEG–x CPT	M _n		CPT content ^b	PEG content ^b	Morphology	IC ₅₀ (μg/mL) ^c		PK parameters	
	Cal.	Found ^a				MCF-7	MCF-7/ADR	AUC (%IDh/g)	t _{1/2} (h)
PEG ₄₅ –CPT	2593	2605	13.4%	77.1%	Sphere	–	–	–	–
PEG ₄₅ –DiCPT	3243	3215	21.4%	61.7%	Sphere	0.138	0.109	47.13	1.61
PEG ₄₅ –TetraCPT	4543	4386	30.6%	44.0%	Rod	0.073	0.065	239.71	5.82
PEG ₄₅ –OctaCPT	7143	6853	38.9%	28.0%	Rod	0.070	0.066	58.2	1.70

^a M_n of PEG₄₅–CPT, PEG₄₅–DiCPT and PEG₄₅–TetraCPT was estimated by MALDI–TOF MS spectra, and M_n of PEG₄₅–OctaCPT was estimated from GPC.

^b Calculated according to the molecular formula.

^c Determined by MTT assays (72 h of culture).

PEG₄₅–CPT, 2.12 for PEG₄₅–DiCPT, 3.83 for PEG₄₅–TetraCPT, and 8.57 for PEG₄₅–OctaCPT. The conjugates contained no free CPT, as confirmed by HPLC and TLC. All these results confirmed their structures (Fig. 2). Table 1 summarizes the characterizations and the properties of these conjugates. Notably, the CPT contents of PEG₄₅–CPT, PEG₄₅–DiCPT, PEG₄₅–TetraCPT and PEG₄₅–OctaCPT were 13.4%, 21.4%, 30.6%, and 38.9% by weight, respectively.

3.2. Self-assembly of PEG–x CPT conjugates

The PEG–x CPT formed nanoparticles at concentrations higher than their CMCs (Table 1; Fig. 6). The morphologies of the nanoparticles in the aqueous solution were observed using TEM (Fig. 7A–D). PEG₄₅–CPT and PEG₄₅–DiCPT formed uniform ~100 nm nanospheres (Fig. 7A and B). Interestingly, PEG₄₅–TetraCPT and PEG₄₅–OctaCPT formed unusual nanorods (Fig. 7C and D). The nanorods of PEG₄₅–TetraCPT were about 60 nm in diameter and 500 nm long, and those of PEG₄₅–OctaCPT were about 100 nm in diameter and about 1 μm long. These structures were further confirmed by confocal fluorescence microscopy after loading with a fluorescent dye Nile red (Fig. 7E–H).

3.3. In vitro stability and drug release

The stability of the nanostructures was studied in PBS at 37 °C by DLS. PEG₄₅–DiCPT nanospheres and PEG₄₅–TetraCPT nanorods were stable for over five days and their sizes did not change over time, whereas PEG₄₅–OctaCPT nanorods aggregated slightly. None of these nanostructures released any CPT under these conditions. However, in the presence of DTT, a strong reducing agent similar to GSH, they immediately released CPT–SH as detected by HPLC (Fig. 8).

3.4. Cellular uptake

An anticancer drug, doxorubicin (DOX), was loaded into the nanocarriers (PEG₄₅–DiCPT/DOX) and nanorods (PEG₄₅–TetraCPT/DOX and PEG₄₅–OctaCPT/DOX) as a tracer study their cell internalization into non- and drug resistant cells using confocal microscopy and flow cytometry (Fig. 9). As shown in Fig. 9A, the cellular uptakes of DOX-loaded nanospheres and nanorods were different from that of free DOX. Free DOX easily entered the non-drug-resistant cells (MCF-7) by passive diffusion [47], as evidenced by the strong fluorescence throughout the cells; only very weak DOX fluorescence was observed in multidrug-resistant cells (MCF-7/ADR) since DOX is a substrate of their drug resistance. In contrast, strong DOX fluorescence was observed in both MCF-7 (data not shown) and MCF-7/ADR cells after they were cultured with DOX-loaded nanoparticles for 1 h, and the intracellular fluorescent intensity increased gradually with the culturing time (4 or 8 h). Two more phenomena were further observed: In MCF-7 cells, the intracellular DOX distributed in the whole cells after 8 h of culturing, including the nuclei; but in MCF-7/ADR cells, the intracellular DOX could not enter the nuclei. Furthermore, the DOX–

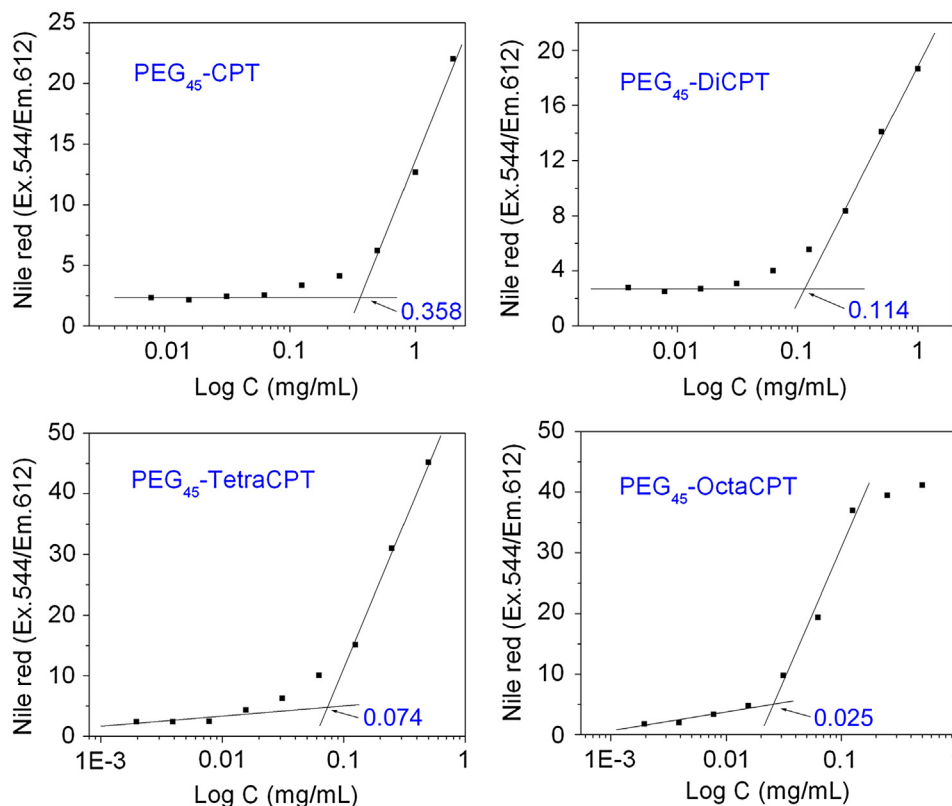


Fig. 6. The CMC values of PEG₄₅-x-CPT determined from the plot of Nile red fluorescence intensity as a function of their concentrations.

intensity of the cells cultured with the nanorods (PEG₄₅-TetraCPT/DOX and PEG₄₅-OctaCPT/DOX) was much higher than those cultured with the nanospheres (PEG₄₅-DiCPT/DOX), particularly those with the PEG₄₅-OctaCPT/DOX nanorods, suggesting much faster cellular uptake of the nanorods than that of the nanospheres. This was further proven by quantitation using flow cytometry (Fig. 9B) in terms of the increase of the mean fluorescence intensity relative to the control. Clearly, at each time point, the cells cultured with nanorods, PEG₄₅-TetraCPT/DOX or PEG₄₅-OctaCPT/DOX, had higher fluorescence intensities than those cultured with the spherical PEG₄₅-DiCPT/DOX (all $P < 0.01$). At 8 h culture, the DOX intensity of the cells cultured with PEG₄₅-TetraCPT/DOX or PEG₄₅-OctaCPT/DOX was 1.15 or 1.39 times that of those cultured with PEG₄₅-DiCPT/DOX.

3.5. Cytotoxicity

The cytotoxicity of free CPT, and the nanospheres/nanorods to MCF-7 or MCF-7/ADR cancer cells was evaluated using the (3-(4,5-dimethylthiazolyl-2)-2,5-diphenyltetrazolium bromide) (MTT) assay (Fig. 10). With 72 h culture, the IC₅₀ value to MCF-7 cells was 0.138 $\mu\text{g/mL}$ for PEG₄₅-DiCPT, 0.073 $\mu\text{g/mL}$ for PEG₄₅-TetraCPT and 0.070 $\mu\text{g/mL}$ for PEG₄₅-OctaCPT, higher than that of CPT. Their IC₅₀ values to MCF-7/ADR cells were not significantly different from those for nonresistant cells since CPT is not the substrate of their drug resistance [48].

3.6. Pharmacokinetics and biodistribution

The pharmacokinetics and biodistribution of nanospheres and nanorods were studied after *i.v.* administration to BALB/c mice. The CPT concentrations in the bloodstream and tissues were determined by HPLC. Fig. 11A shows the blood clearance profiles. PEG₄₅-TetraCPT

was cleared slowly and there was still $3.59 \pm 0.29\%$ of the injected dose per gram of blood after 24 h. In contrast, after 8 h, PEG₄₅-DiCPT nanospheres or PEG₄₅-OctaCPT nanorods were barely detected in the blood. Elimination half-life times ($t_{1/2, \beta}$) of the nanostructures were calculated using a two-compartment model (Table 1). The $t_{1/2}$ of PEG₄₅-TetraCPT (5.82 h) was significantly greater than those of PEG₄₅-DiCPT (1.61 h) and PEG₄₅-OctaCPT (1.70 h). Correspondingly, the area-under-the-curve value for 24 h ($AUC_{0-24 \text{ h}}$) of PEG₄₅-TetraCPT was 4–5 times larger than those of PEG₄₅-DiCPT and PEG₄₅-OctaCPT. Thus, PEG₄₅-TetraCPT nanorods had a much better stealth property than the PEG₄₅-DiCPT nanospheres.

The biodistributions of the nanostructures in terms of CPT concentration in different organs of mice at 4 and 24 h post *i.v.* administration are shown in Fig. 11B and C. At 4 h, the nanostructures were mainly found in the spleen. In addition, some PEG₄₅-DiCPT accumulated in the liver ($15.75 \pm 3.85\%$ ID/g tissue) and a significant amount of PEG₄₅-OctaCPT nanorods was in the lung ($64.89 \pm 2.63\%$). Thus, the liver and spleen were still responsible for the clearance of the nanospheres and nanorods. The long PEG₄₅-OctaCPT nanorods also accumulated in lung, explaining its shorter blood-circulation time compared to PEG₄₅-TetraCPT nanorods. Clearly, PEG₄₅-TetraCPT had lower concentrations in liver and spleen than PEG₄₅-DiCPT, consistent with the results in Fig. 11A. After 24 h, PEG₄₅-DiCPT almost disappeared from all the organs. The level of PEG₄₅-OctaCPT in the lung was also greatly reduced and little remained in the spleen ($10.53 \pm 1.31\%$ ID/g of tissue) and liver ($3.55 \pm 0.57\%$ ID/g tissue). PEG₄₅-TetraCPT was still found in the spleen ($22.05 \pm 6.33\%$ ID/g tissue) and blood ($3.59 \pm 0.29\%$ ID/g blood).

3.7. Ex vivo imaging

Ex vivo imaging of excised tissues and tumors at 8 h post-injection further confirmed the results (Fig. 12). The mice injected

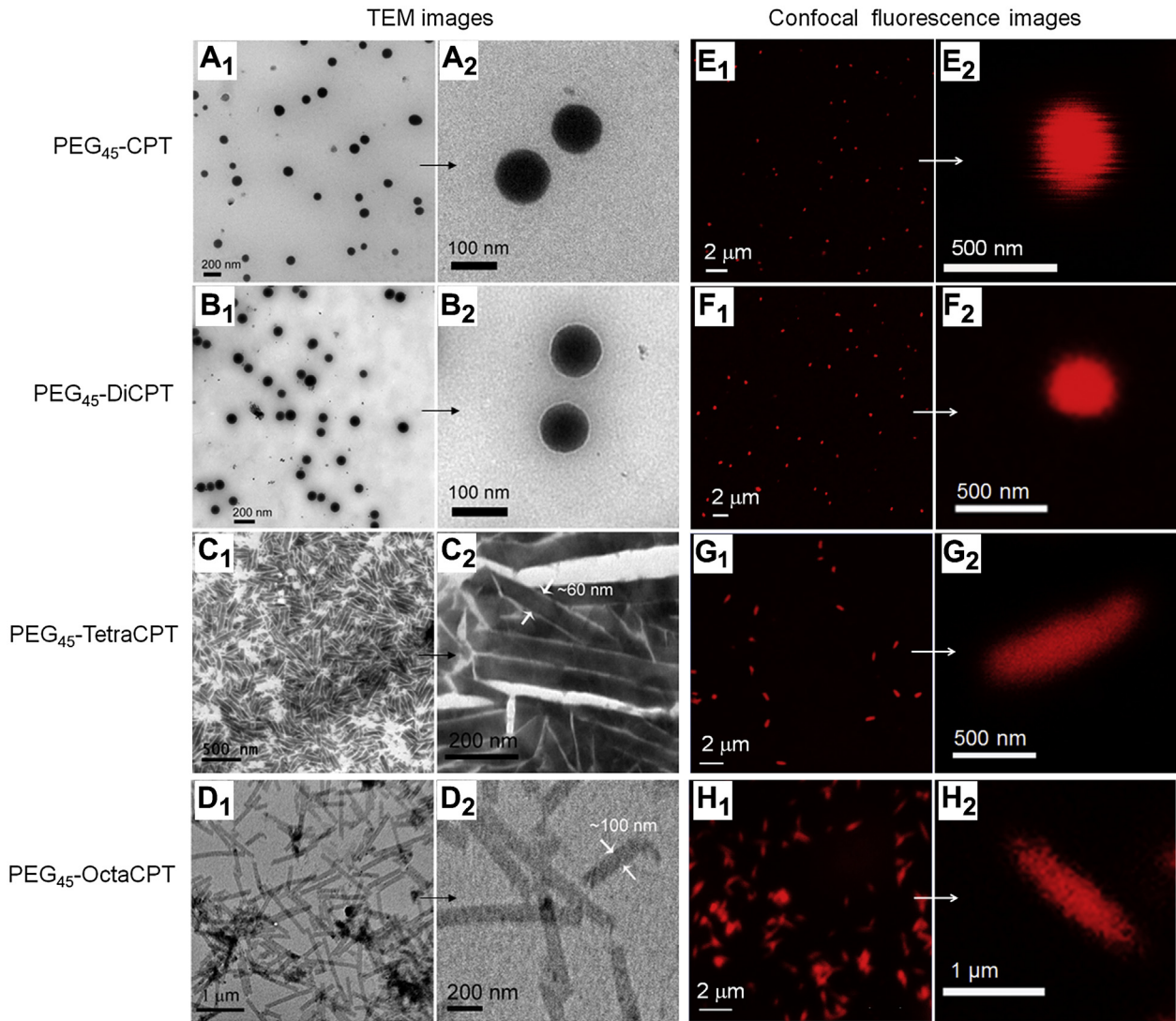


Fig. 7. The TEM and confocal fluorescence images and their corresponding enlarged ones of PEG₄₅-CPT (A, E) PEG₄₅-DiCPT (B, F), PEG₄₅-TetraCPT (C, G), PEG₄₅-OctaCPT (D, H) formed nanostructures. The nanostructures were loaded with 1% Nile red for taking corresponding confocal fluorescence images.

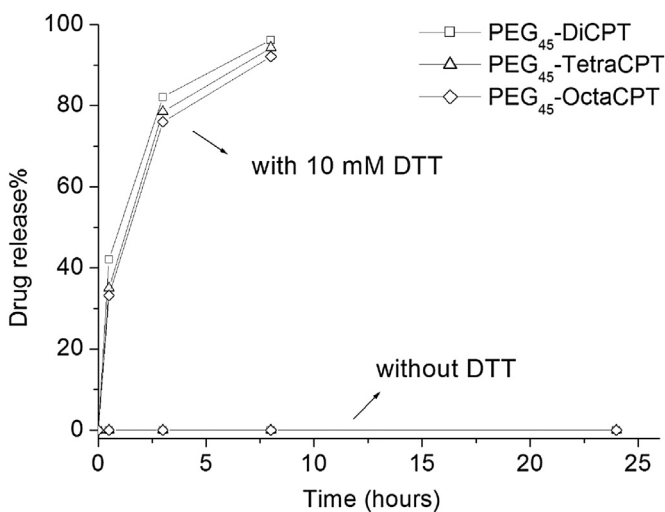


Fig. 8. The corresponding time dependent CPT-SH release of PEG-xCPT nanoparticles treated with or without 10 mM DTT.

with PEG₄₅-DiCPT/DOX nanospheres or PEG₄₅-OctaCPT/DOX nanorods had higher DOX-fluorescence in livers than those injected with PEG₄₅-TetraCPT/DOX nanorods. The mice injected with PEG₄₅-OctaCPT/DOX nanorods also had stronger DOX-fluorescence in the lung. Very low fluorescence was observed in the heart and spleen for all the mice. Side-by-side imaging of the tumors from the mice injected with PEG₄₅-DiCPT/DOX or PEG₄₅-TetraCPT/DOX nanorods is shown in Fig. 12B. The Student *t*-test indicated that the DOX-fluorescence in the tumors from mice injected with nanospheres and nanorods was statistically different. Fluorescence intensity in the tumors of the mice injected with PEG₄₅-TetraCPT/DOX nanorods was 2.8 times that of those injected with PEG₄₅-DiCPT/DOX nanospheres.

4. Discussion

For a nanocarrier to achieve a high therapeutic efficacy, the key is not to emphasize one but to reconcile and unite the opposite requirements: long blood circulation and tight drug retention while in the blood compartment, but fast cellular uptake and intracellular drug release once in the tumor [23]. Toward this end, we hoped to combine the characters of worm micelles' long circulation [5], drug

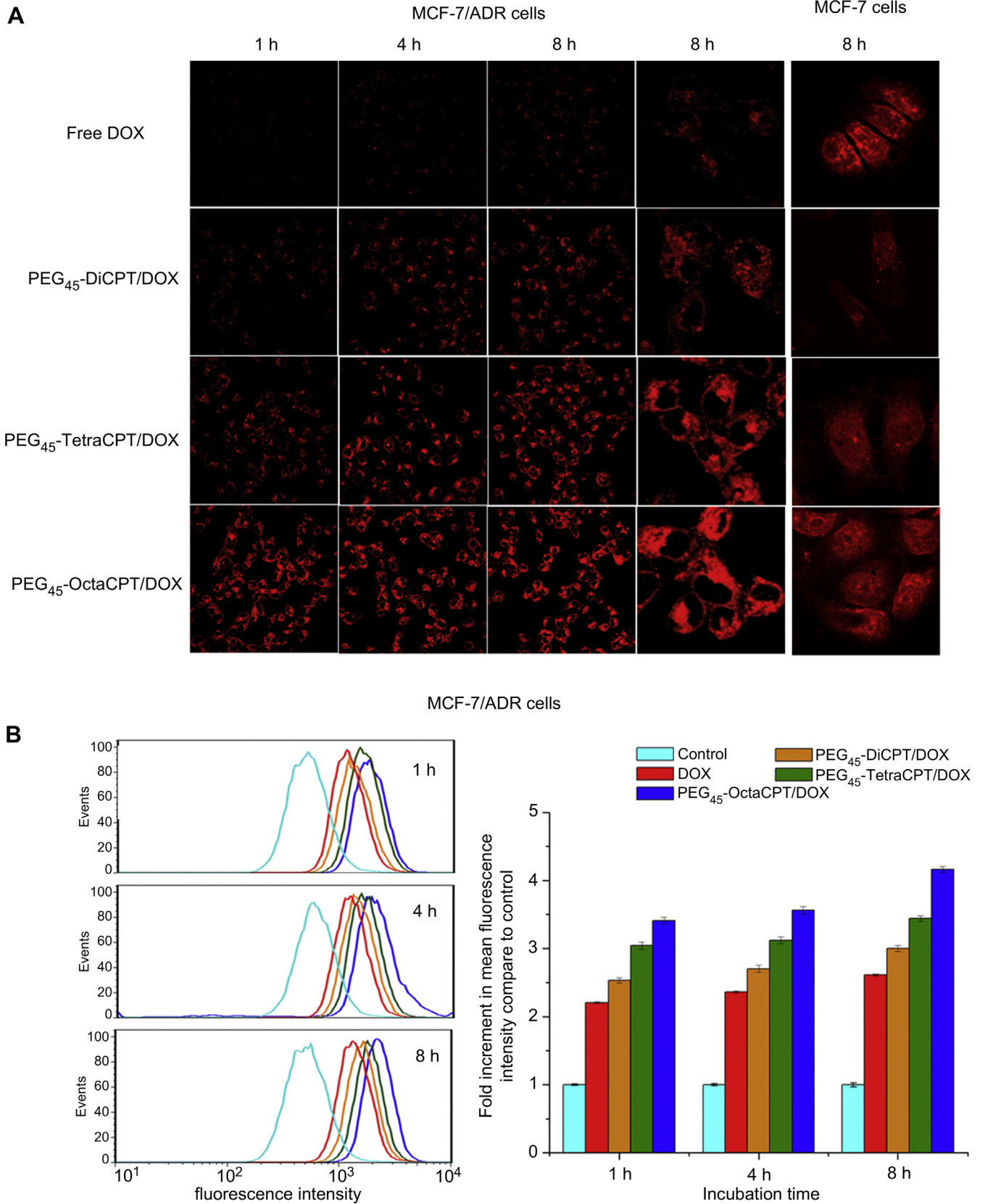


Fig. 9. Cellular uptake study of free DOX, PEG₄₅-DiCPT/DOX, PEG₄₅-TetraCPT/DOX and PEG₄₅-OctaCPT/DOX by confocal microscopy (A) and flow cytometry (B). The free DOX and the DOX-loaded nanostructures (DOX dose: 4 μg/mL) were cultured individually with MCF-7 or MCF-7/ADR cancer cells at 37 °C for 1, 4 or 8 h.

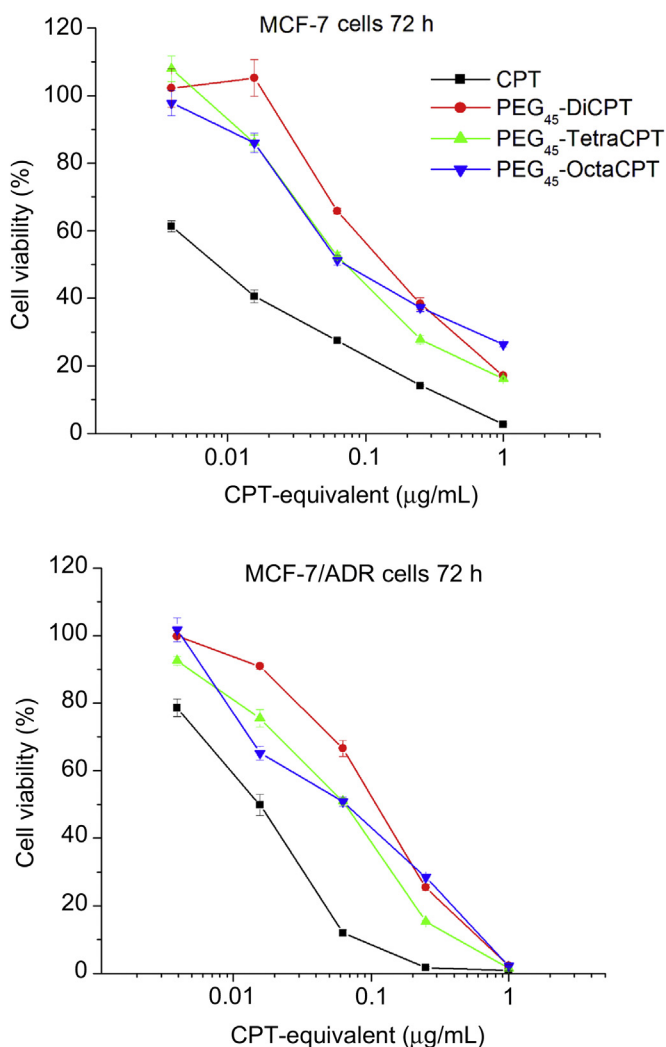


Fig. 10. The cytotoxicity of free CPT and PEG₄₅-x-CPT to MCF-7 or MCF-7/ADR cells after 72 h culture estimated by MTT assay. Data represent mean \pm s.d., $n = 5$.

conjugates' intracellular-triggered drug release [43,49–51], and nanorods' fast cellular uptake [33–35] and tumor penetration [32] into biodegradable polymer nanorods. Such drug-conjugate nanorods have not been achieved from self-assembly of amphiphilic copolymers because of the narrow composition window and the strict requirements on the polymer structure for forming this morphology [39,41,52].

Linear-dendritic amphiphilic block copolymers can self-assemble into various morphologies by tuning their hydrophobic dendritic generations [40], and the formed spherical nanoparticles were useful for drug loading [46,53]. We conjugated hydrophobic CPT to a water-soluble PEG–DPLL block copolymer to make amphiphilic linear-dendritic conjugates, PEG–x-CPT, and hoped that by tailoring the generation of the DPLL and thus the number of conjugated CPT molecules (x), we could fine-tune the hydrophilic/hydrophobic balance of the amphiphilic conjugates to form the desired nanostructures. Such conjugates would also be advantageous for their well-defined molecular structures with precisely controlled numbers of CPT moieties, as shown in Figs. 3–5. Consequently, the drug loading content of each nanostructure is fixed independently of the fabrication process, which is very important for future development and clinical translation [23]. Furthermore, compared to the physical drug loading systems whose drug contents are usually lower than 10% to minimize the initial burst release [7,24], the

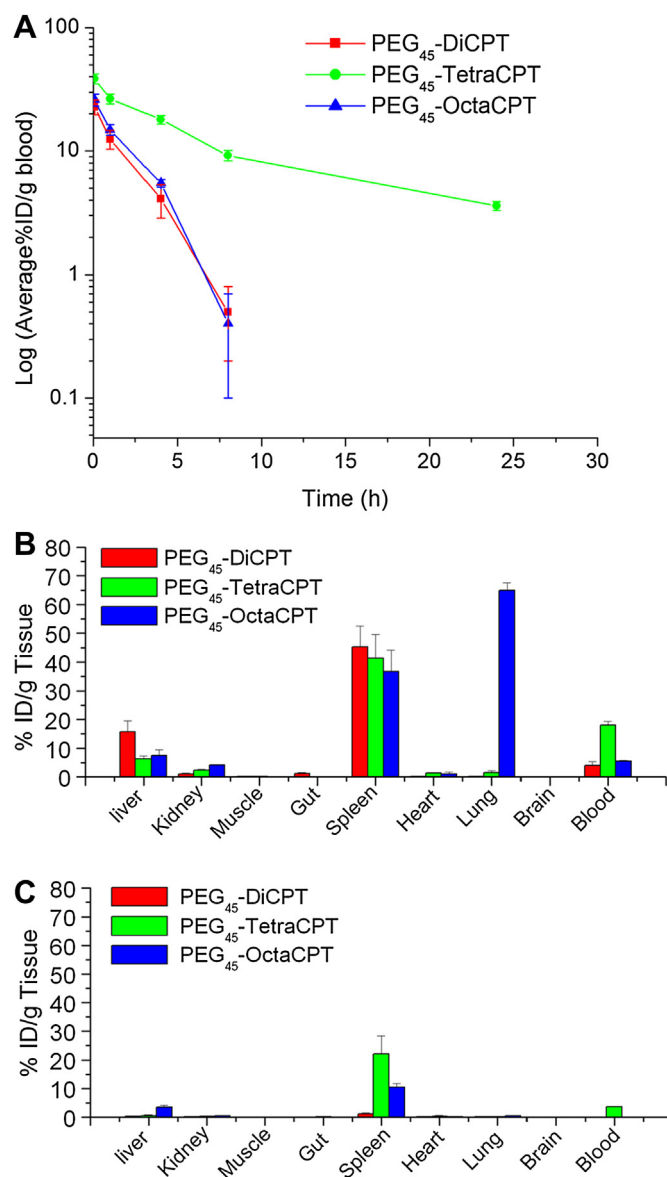


Fig. 11. The blood clearance profiles (A) and biodistribution at 4 h (B) or 24 h (C) post i.v. administration of the PEG₄₅-x-CPT nanostructures. Dose, 10 mg CPT-eq./kg, $n = 4$.

formed nanostructures from PEG–x-CPT had high drug loading contents, 21 wt% for PEG₄₅-DiCPT and 30.6 wt% for PEG₄₅-TetraCPT (Table 1).

PEG–x-CPT indeed formed spherical- to rod-like nanostructures determined by the number of the conjugated-CPT molecules (x ; Fig. 2, Table 1). The conjugates with one or two CPT molecules, whose hydrophilic PEG contents were 77.1 wt% or 61.7 wt% (Table 1), formed nanospheres around 100 nm, as confirmed by TEM (Fig. 7). The conjugates with four (44 wt% PEG) or eight CPT molecules (28 wt% PEG) formed rodlike rather than flexible wormlike micelles. The nanorods had very uniform diameters and lengths. Those from PEG₄₅-TetraCPT were about 60 nm in diameter and about 500 nm long; those from PEG₄₅-OctaCPT were doubled in both diameter and length. These nanorods without any bending looked much like rigid gold or inorganic nanorods [30,54], as a result of the very tight packing of the DPLL–x-CPT blocks owing to the hydrogen bonding among the amide groups and strong π – π stacking of the CPT moieties [10]. In contrast, PEG–PCL and PEG–PLA copolymers formed flexible worm-like micelles [36,38–40] due to their fluid cores [41,42].

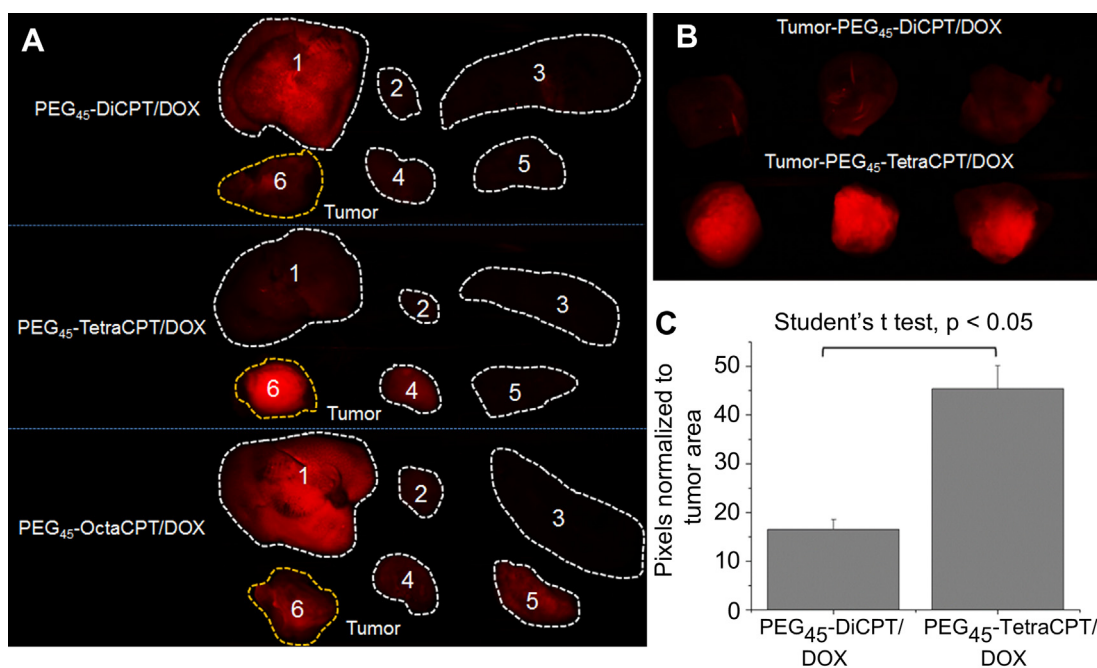


Fig. 12. Ex vivo imaging of the biodistribution and tumor accumulation of the nanostructures. Mice bearing 4T1-Luc breast tumors ($\sim 300 \text{ mm}^3$) were intravenously injected with DOX-loaded nanostructures (5 mg DOX-equivalent/kg body weight). After 8 h, the mice were sacrificed and the tumors and various organs (1. Liver, 2. Heart, 3. Spleen, 4. Kidney, 5. Lung, 6. Tumor) were imaged with the Maestro FLEX In Vivo Imaging System (A). The three tumors of mice in each group injected with PEG₄₅-DiCPT/DOX or PEG₄₅-TetraCPT/DOX were further imaged side-by-side (B) and their pixels were normalized to tumor area using the Maestro software (C).

The PEG₄₅-DiCPT nanospheres and PEG₄₅-TetraCPT nanorods were stable in PBS without any change in size. The PEG₄₅-OctaCPT nanorods, however, slowly aggregated in PBS due to their large particle size. The CPT moieties were conjugated via disulfide bonds, so they did not release any CPT but could be cleaved intracellularly by GSH [43], as evidenced by the aggregation and the release of the CPT (Fig. 8) upon the addition of DTT.

Once cultured with cells, both the nanospheres and nanorods were taken up into the cells within less than an hour. These nanoparticles dramatically increased intracellular accumulation of DOX in MCF-7/ADR cells compared to free DOX. Obviously, the nanorods (PEG₄₅-TetraCPT/DOX and PEG₄₅-OctaCPT/DOX), particularly the long nanorods, were taken up more rapidly than the nanospheres (PEG₄₅-DiCPT/DOX) (Fig. 9). Since nanospheres and nanorods had exactly the same surface characters, such facilitated cellular uptake must be due to the elongated shape of the nanorods. This is consistent with the fast cellular uptake found in metallic or inorganic nanorods [33,55,56]. The fast cellular uptake of the nanorods might result from their larger surface area [33,57], but its exact underlying mechanism is still under study. Furthermore, when cultured with non-drug-resistant cells (MCF-7), DOX carried by PEG- χ CPT nanospheres or nanorods distributed throughout the cells, including the nuclei, similarly to free DOX. This suggests that once the PEG- χ CPT nanostructures were inside the cells, intracellular GSH cleaved their disulfide bonds and released the hydrophobic CPT moieties, leading to dissolving the particles and releasing the DOX. However, DOX carried by the nanostructures could not enter the nuclei of the multidrug-resistant cells (MCF-7/ADR) due to the outward drug transport by drug resistance on their nuclear membrane [58].

PEG₄₅- χ CPT had comparable cytotoxicity with free CPT (Fig. 10). The water-soluble GSH could diffuse into the nanostructures' tight hydrophobic core and CPT moieties were cleaved from the tightly packed nanoparticles. However, GSH cleaved the disulfide bonds and released the CPT-thioester (CPT-SH); the CPT-SH had to further

hydrolyze to the parent CPT to exert the pharmaceutical effects [59]. Consistent with the cellular uptake results, the PEG₄₅-TetraCPT and PEG₄₅-OctaCPT had cytotoxicity higher than that of PEG₄₅-DiCPT.

The blood-circulation time of PEG₄₅-TetraCPT nanorods was much longer than that of the PEG₄₅-DiCPT nanospheres (Fig. 11A) as well as their AUC value, confirming our hypothesis. Again, since the PEG₄₅-DiCPT nanospheres and PEG₄₅-TetraCPT nanorods were identical in their surface chemistry and close in their volumes, the prolonged circulation time of the nanorods must be due to their elongated shape, which might align or tumble in the flow to reduce clearance by the liver or spleen [14]. Indeed, the PEG₄₅-TetraCPT nanorods were sequestered in the liver about one-third as much as the PEG₄₅-DiCPT nanospheres at 4 h after administration (Fig. 11B). The sequestration into the spleen was very similar for the three nanostructures and much higher than that in the liver. These spleen sequestration was due to their rigidity. It is known that rigid structures are easily subject to splenic filtration in the venous sinuses [14] because, compared to their flexible wormlike counterparts, they are less able to deform to navigate the physical filtration barriers in the body [60]. This may be the main reason that the PEG₄₅-TetraCPT nanorods were cleared more quickly than the flexible worm-like micelles [5–7]. The more elongated nanorods from PEG₄₅-OctaCPT were also captured by the lung, shortening their circulation time, but the lung filtration of PEG₄₅-TetraCPT nanorods was avoided. This is the first direct evidence that nanorods with the proper sizes may have greater blood circulation than corresponding nanospheres.

The tumor accumulation of PEG₄₅-TetraCPT/DOX was much more than PEG₄₅-DiCPT/DOX or PEG₄₅-OctaCPT/DOX (Fig. 12) due to its prolonged blood circulation. Faster cellular uptake of the nanorods than nanospheres in the tumor might also account for this result. PEG₄₅-TetraCPT/DOX also showed lower uptake in the liver, further confirming that short nanorods have reduced reticuloendothelial system (RES) uptake.

Thus, the PEG₄₅–TetraCPT nanorods had simultaneously good stealth properties and fast cellular uptake compared to nanospheres. These two characters are essential for efficient cancer-drug delivery but are generally difficult to unite in one nanocarrier since stealth properties are generally achieved by preventing cellular uptake. Furthermore, unlike metallic and inorganic nanorods [30,54], these nanorods were biodegradable for excretion, which is also essential for future clinic translation.

5. Conclusion

In summary, we demonstrated a facile approach to fabricating polymer–drug–conjugate nanorods for cancer-drug delivery. Using a hydrophobic drug as the hydrophobic moiety, we synthesized well-defined amphiphilic linear-dendritic drug conjugates, PEG-*b*-dendritic polylysine–CPT. Tailoring their generation and the number of the conjugated CPT molecules induced the linear-dendritic conjugates to self-assemble into spherical- or rod-like nanostructures stable at the physiological conditions but quickly releasing the drug CPT once in the cytosol. The shape of the nanostructures affected their cellular uptake and *in vivo* blood clearance. The nanorods were taken up more efficiently by cancer cells than nanospheres. The nanorods with medium lengths (<500 nm) also had a much better stealth property and thus a much longer blood circulation than the nanospheres. However, micrometer-long nanorods were easily removed from the bloodstream by RES clearance and lung accumulation. Thus, this work demonstrates that pegylated conjugate nanorods with proper lengths can unite the two opposites in cancer-drug delivery—long blood circulation *versus* fast cellular uptake and drug retention in circulation *versus* intracellular drug release, ideal for efficient tumor-drug delivery.

Acknowledgment

The authors thank the Major Program of National Natural Science Foundation of China (21090352), the National Natural Science Foundation (20974096, 21104065), the National Fund for Distinguished Young Scholars (50888001), the Program for Changjiang Scholars and Innovative Research Team in the University of China, and the U.S. Department of Defense (BC090502) for financial support.

References

- [1] Bae Y, Kataoka K. Intelligent polymeric micelles from functional poly(ethylene glycol)-poly(amino acid) block copolymers. *Adv Drug Deliv Rev* 2009;61:768–84.
- [2] Lippard SJ, Dhar S, Gu FX, Langer R, Farokhzad OC. Targeted delivery of cisplatin to prostate cancer cells by aptamer functionalized Pt(IV) prodrug-PLGA-PEG nanoparticles. *Proc Natl Acad Sci U S A* 2008;105:17356–61.
- [3] Xiao Y, Hong H, Javadi A, Engle JW, Xu W, Yang Y, et al. Multifunctional unimolecular micelles for cancer-targeted drug delivery and positron emission tomography imaging. *Biomaterials* 2012;33:3071–82.
- [4] Zhou K, Wang Y, Huang X, Luby-Phelps K, Sumer BD, Gao J. Tunable, ultrasensitive pH-responsive nanoparticles targeting specific endocytic organelles in living cells. *Angew Chem Int Ed* 2011;50:6109–14.
- [5] Geng Y, Dalhaimer P, Cai SS, Tsai R, Tewari M, Minko T, et al. Shape effects of filaments versus spherical particles in flow and drug delivery. *Nat Nanotechnol* 2007;2:249–55.
- [6] Christian DA, Cai SS, Garbuzenko OB, Harada T, Zajac AL, Minko T, et al. Flexible filaments for *in vivo* imaging and delivery: persistent circulation of filomicelles opens the dosage window for sustained tumor shrinkage. *Mol Pharm* 2009;6:1343–52.
- [7] Loverde SM, Klein ML, Discher DE. Nanoparticle shape improves delivery: rational coarse grain molecular dynamics (rCG-MD) of taxol in worm-like PEG-PCL micelles. *Adv Mater* 2011;24:3823–30.
- [8] Discher DE, Eisenberg A. Polymer vesicles. *Science* 2002;297:967–73.
- [9] Discher DE, Ahmed F. Polymersomes. *Annu Rev Biomed Eng* 2006;8:323–41.
- [10] Shen Y, Jin E, Zhang B, Murphy CJ, Sui M, Zhao J, et al. Prodrugs forming high drug loading multifunctional nanocapsules for intracellular cancer drug delivery. *J Am Chem Soc* 2010;132:4259–65.
- [11] Jain RK. Delivery of molecular medicine to solid tumors: lessons from *in vivo* imaging of gene expression and function. *J Control Release* 2001;74:7–25.
- [12] Davis ME, Chen Z, Shin DM. Nanoparticle therapeutics: an emerging treatment modality for cancer. *Nat Rev Drug Discov* 2008;7:771–82.
- [13] Torchilin V. Tumor delivery of macromolecular drugs based on the EPR effect. *Adv Drug Deliv Rev* 2011;63:131–5.
- [14] Moghimi SM, Hunter AC, Murray JC. Long-circulating and target-specific nanoparticles: theory to practice. *Pharmacol Rev* 2001;53:283–318.
- [15] Ma LL, Jie P, Venkatraman SS. Block copolymer 'stealth' nanoparticles for chemotherapy: interactions with blood cells *in vitro*. *Adv Funct Mater* 2008;18:716–25.
- [16] Alexis F, Pridgen E, Molnar LK, Farokhzad OC. Factors affecting the clearance and biodistribution of polymeric nanoparticles. *Mol Pharm* 2008;5:505–15.
- [17] Yoo JW, Chambers E, Mitragotri S. Factors that control the circulation time of nanoparticles in blood: challenges, solutions and future prospects. *Curr Pharm Des* 2010;16:2298–307.
- [18] Zhu Z, Xie C, Liu Q, Zhen X, Zheng X, Wu W, et al. The effect of hydrophilic chain length and iRGD on drug delivery from poly(ϵ -caprolactone)-poly(*N*-vinylpyrrolidone) nanoparticles. *Biomaterials* 2011;32:9525–35.
- [19] Cabral H, Matsumoto Y, Mizuno K, Chen Q, Murakami M, Kimura M, et al. Accumulation of sub-100 nm polymeric micelles in poorly permeable tumors depends on size. *Nat Nanotechnol* 2011;6:815–23.
- [20] Fox ME, Szoka FC, Fréchet JMJ. Soluble polymer carriers for the treatment of cancer: the importance of molecular architecture. *Acc Chem Res* 2009;42:1141–51.
- [21] Prencipe G, Tabakman SM, Welscher K, Liu Z, Goodwin AP, Zhang L, et al. PEG branched polymer for functionalization of nanomaterials with ultralong blood circulation. *J Am Chem Soc* 2009;131:4783–7.
- [22] Venkataraman S, Hedrick JL, Ong ZY, Yang C, Ee PLR, Hammond PT, et al. The effects of polymeric nanostructure shape on drug delivery. *Adv Drug Deliv Rev* 2011;63:1228–46.
- [23] Sun Q, Radosz M, Shen Y. Challenges in design of translational nanocarriers. *J Control Release* 2012;164:156–69.
- [24] Geng Y, Discher DE. Visualization of degradable worm micelle breakdown in relation to drug release. *Polymer* 2006;47:2519–25.
- [25] Allen TM, Cullis PR. Drug delivery systems: entering the mainstream. *Science* 2004;303:1818–22.
- [26] Champion JA, Mitragotri S. Role of target geometry in phagocytosis. *Proc Natl Acad Sci U S A* 2006;103:4930–4.
- [27] Champion JA, Mitragotri S. Shape induced inhibition of phagocytosis of polymer particles. *Pharm Res* 2009;26:244–9.
- [28] Decuzzi P, Godin B, Tanaka T, Lee SY, Chiappini C, Liu X, et al. Size and shape effects in the biodistribution of intravascularly injected particles. *J Control Release* 2010;141:320–7.
- [29] Hubbell JA, Chilkoti A. Nanomaterials for drug delivery. *Science* 2012;337:303–5.
- [30] Wijaya A, Schaffer SB, Pallares IG, Hamad-Schifferli K. Selective release of multiple DNA oligonucleotides from gold nanorods. *ACS Nano* 2009;3:80–6.
- [31] Yue ZG, Wei W, You ZX, Yang QZ, Yue H, Su ZG, et al. Iron oxide nanotubes for magnetically guided delivery and pH-activated release of insoluble anticancer drugs. *Adv Funct Mater* 2011;21:3446–53.
- [32] Chauhan VP, Popovic Z, Chen O, Cui J, Fukumura D, Bawendi MG, et al. Fluorescent nanorods and nanospheres for real-time *in vivo* probing of nanoparticle shape-dependent tumor penetration. *Angew Chem Int Ed* 2011;50:11417–20.
- [33] Gratton SEA, Ropp PA, Pohlhaus PD, Luft JC, Madden VJ, Napier ME, et al. The effect of particle design on cellular internalization pathways. *Proc Natl Acad Sci U S A* 2008;105:11613–8.
- [34] Petros RA, DeSimone JM. Strategies in the design of nanoparticles for therapeutic applications. *Nat Rev Drug Discov* 2010;9:615–27.
- [35] Meng H, Yang S, Li Z, Xia T, Chen J, Ji Z, et al. Aspect ratio determines the quantity of mesoporous silica nanoparticle uptake by a small GTPase-dependent macropinocytosis mechanism. *ACS Nano* 2011;5:4434–47.
- [36] Takeoka S, Mori K, Ohkawa H, Sou K, Tsuchida E. Synthesis and assembly of poly(ethylene glycol)-lipids with mono-, di-, and tetraacyl chains and a poly(ethylene glycol) chain of various molecular weights. *J Am Chem Soc* 2000;122:7927–35.
- [37] Pati D, Kalva N, Das S, Kumaraswamy G, Sen Gupta S, Ambade AV. Multiple topologies from glycopolymer-dendron conjugate self-assembly: nanorods, micelles, and organogels. *J Am Chem Soc* 2012;134:7796–802.
- [38] Kim Y, Dalhaimer P, Christian DA, Discher DE. Polymeric worm micelles as nano-carriers for drug delivery. *Nanotechnology* 2005;16:S484–91.
- [39] Jain S, Bates FS. On the origins of morphological complexity in block copolymer surfactants. *Science* 2003;300:460–4.
- [40] del Barrio J, Oriol L, Sanchez C, Serrano JL, Di Cicco A, Keller P, et al. Self-assembly of linear-dendritic diblock copolymers: from nanofibers to polymersomes. *J Am Chem Soc* 2010;132:3762–9.
- [41] Geng Y, Discher DE. Hydrolytic degradation of poly(ethylene oxide)-block-polycaprolactone worm micelles. *J Am Chem Soc* 2005;127:12780–1.
- [42] Balsamo V, de Navarro CU, Gil G. Microphase separation vs crystallization in polystyrene-*b*-polybutadiene-*b*-poly(epsilon-caprolactone) ABC triblock copolymers. *Macromolecules* 2003;36:4507–14.
- [43] Zhou Z, Shen Y, Tang J, Fan M, Van Kirk EA, Murdoch WJ, et al. Charge-reversal drug conjugate for targeted cancer cell nuclear drug delivery. *Adv Funct Mater* 2009;19:3580–9.

- [44] Xie HZ, Braha O, Gu LQ, Cheley S, Bayley H. Single-molecule observation of the catalytic subunit of cAMP-dependent protein kinase binding to an inhibitor peptide. *Chem Biol* 2005;12:109–20.
- [45] Chapman TM, Hillyer GL, Mahan EJ, Shaffer KA. Hydraamphiphiles: novel linear dendritic block copolymer surfactants. *J Am Chem Soc* 1994;116:11195–6.
- [46] Gillies ER, Jonsson TB, Fréchet JM. Stimuli-responsive supramolecular assemblies of linear-dendritic copolymers. *J Am Chem Soc* 2004;126:11936–43.
- [47] Yoo HS, Park TG. Biodegradable polymeric micelles composed of doxorubicin conjugated PLGA-PEG block copolymer. *J Control Release* 2001;70:63–70.
- [48] Sinha BK, Katki AG, Batist G, Cowan KH, Myers CE. Differential formation of hydroxyl radicals by adriamycin in sensitive and resistant MCF-7 human-breast tumor-cells – implications for the mechanism of action. *Biochemistry* 1987;26:3776–81.
- [49] Harada M, Bobe I, Saito H, Shibata N, Tanaka R, Hayashi T, et al. Improved anti-tumor activity of stabilized anthracycline polymeric micelle formulation, NC-6300. *Cancer Sci* 2011;102:192–9.
- [50] Bae Y, Ponta A. PEG-poly(amino acid) block copolymer micelles for tunable drug release. *Pharm Res* 2010;27:2330–42.
- [51] Aryal S, Hu CMJ, Zhang L. Polymer-cisplatin conjugate nanoparticles for acid-responsive drug delivery. *ACS Nano* 2010;4:251–8.
- [52] Wang Y, Xu H, Zhang X. Tuning the amphiphilicity of building blocks: controlled self-assembly and disassembly for functional supramolecular materials. *Adv Mater* 2009;21:2849–64.
- [53] Xiao K, Fowler WL, Li YP, Lee JS, Xing L, Cheng RH, et al. A self-assembling nanoparticle for paclitaxel delivery in ovarian cancer. *Biomaterials* 2009;30:6006–16.
- [54] Giri S, Trewyn BG, Stellmaker MP, Lin VSY. Stimuli-responsive controlled-release delivery system based on mesoporous silica nanorods capped with magnetic nanoparticles. *Angew Chem Int Ed* 2005;44:5038–44.
- [55] Huang X, Teng X, Chen D, Tang F, He J. The effect of the shape of mesoporous silica nanoparticles on cellular uptake and cell function. *Biomaterials* 2010;31:438–48.
- [56] Park JH, von Maltzahn G, Zhang L, Schwartz MP, Ruoslahti E, Bhatia SN, et al. Magnetic iron oxide nanoworms for tumor targeting and imaging. *Adv Mater* 2008;20:1630–5.
- [57] Vácha R, Martínez-Veracoechea FJ, Frenkel D. Receptor-mediated endocytosis of nanoparticles of various shapes. *Nano Lett* 2011;11:5391–5.
- [58] Molinari A, Calcabrini A, Meschini S, Stringaro A, Crateri P, Toccaceli L, et al. Subcellular detection and localization of the drug transporter P-glycoprotein in cultured tumor cells. *Curr Protein Pept Sci* 2002;3:653–70.
- [59] Shen Y, Zhou Z, Sui M, Tang J, Xu P, Van Kirk EA, et al. Charge-reversal polyamidoamine dendrimer for cascade nuclear drug delivery. *Nanomedicine UK* 2010;5:1205–17.
- [60] Merkel TJ, Jones SW, Herlihy KP, Kersey FR, Shields AR, Napier M, et al. Using mechanobiological mimicry of red blood cells to extend circulation times of hydrogel microparticles. *Proc Natl Acad Sci U S A* 2011;108:586–91.